Advanced Functional Materials

ADVANCED FUNCTIONAL MATERIALS
www.afm-journal.de

RESEARCH ARTICLE

Engineering-Free Deterministic Spin-Orbit Torque Switching in Ultrathin Perpendicular Synthetic Antiferromagnets

Wang Yao[1] | Meiling Xu[1] | Yadong Liu[1] | Feiyan Hou[1] | Tao Li[1,2] | Tai Min[1,2,3]

[1]Center For Spintronics and Quantum Systems, State Key Laboratory For Mechanical Behavior of Materials, Department of Materials Science and Engineering, Xi'an Jiaotong University, Xi'an, Shaanxi, China | [2]FZU-Jinjiang Joint Institute of Microelectronics, Jinjiang Campus, Fuzhou University, Jinjiang, China | [3]School of Advanced Manufacturing Engineering, State Key Laboratory of Solid State Microstructures, Nanjing University, Suzhou, China

Correspondence: Tao Li (taoli66@xjtu.edu.cn) | Tai Min (tai.min@nju.edu.cn)

Received: 12 December 2025 | **Revised:** 23 July 2026 | **Accepted:** 30 July 2026

Keywords: antiferromagnetism | condensed matter physics | magnetic field | magnetization | materials science | perpendicular | point reflection | spintronics | symmetry breaking

ABSTRACT

Spin-orbit torque (SOT) offers a promising route for energy-efficient magnetization manipulation in low-power spintronic devices. Synthetic antiferromagnet (SAF) structure, in particular, enhances device performance through ultrafast magnetization switching and magnetic stray-field resilience. However, achieving deterministic SOT switching in perpendicularly magnetized SAFs typically requires an additional in-plane magnetic field or structural engineering to break inversion symmetry, which complicates their practical implementation. Here, we demonstrate field-free deterministic SOT switching in ultra-thin perpendicular SAFs operating at room temperature, designed with a symmetric CoFeB (0.6 nm)/W/CoFeB (0.6 nm) structure. This switching occurs only under antiferromagnetic coupling conditions between the two CoFeB layers, and the switching chirality can be tuned via the spacer layer thickness and temperature. Micromagnetic modeling reveals that symmetry breaking arises intrinsically from the interplay between Ruderman-Kittel-Kasuya-Yosida and Dzyaloshinskii-Moriya interactions, which stabilize the asymmetric Néel-Bloch mixed domain walls of both CoFeB layers. These domain walls manifest as dynamic spin textures with a net chiral driving force, enabling deterministic magnetization switching without the need for external fields or engineered structural asymmetry. Our findings provide a streamlined path toward practical applications of ultrathin SAFs in structurally simplified, fabrication-friendly SOT memory and logic devices.

1 | Introduction

Rapidly advancing spintronic technologies enable ultralow-power non-volatile magnetic random-access memory (MRAM) with enhanced scaling and stability [1–3]. A key enabler of this progress is spin-orbit torque (SOT), a mechanism that leverages strong spin-orbit coupling, typically in heavy-metal (HM) layers, to convert charge currents into spin currents, thereby enabling ultrafast and energy-efficient magnetization manipulation [4–7]. Recent advancements have demonstrated that SOT-MRAM offers superior operational performance compared to spin-transfer torque MRAM, with faster switching speeds, reduced power consumption, improved reliability, and distinct decoupling between read and write paths [8–13]. However, a fundamental requirement for achieving deterministic perpendicular magnetization switching via SOT (generated by bulk spin Hall effects [14–16] or interfacial Rashba-Edelstein effects [17–20]) is the breaking of inversion symmetry to establish a specific spin polarization orientation relative to the magnetization.

A typical SOT-based magnetic tunnel junction (MTJ), the key functional element of MRAM, comprises a ferromagnetic free layer interfaced with a heavy-metal layer. Compared to ferromagnetic free layers, synthetic antiferromagnets (SAFs) have emerged as a superior free-layer architecture, offering multifunctional advantages including enhanced thermal stability, reduced switching current density, suppressed stray fields, and accelerated switching dynamics [21–26]. However, effectively harnessing SOT in SAF-based MTJs imposes stringent requirements on the HM spacer materials used to generate the spin current and mediate Ruderman-Kittel-Kasuya-Yosida (RKKY) coupling. Pt and Ta are commonly used as heavy-metal layers in previous work [27–29]. Nevertheless, inherent limitations constrain their applicability in SAF-based SOT systems, such as that Pt suffers from a low spin Hall angle and extremely low RKKY coupling capability [29–31], whereas Ta exhibits similarly limited spin Hall conductivity despite its RKKY-mediated interaction [30, 31]. In contrast, tungsten (W) demonstrates superior potential as a spacer material for SAF architectures. Its CMOS compatibility, coupled with a pronounced spin Hall angle and robust RKKY interaction generation [30–32], makes W a promising solution for future SOT-based spintronic memory and logic devices.

Despite these benefits, the mandatory use of an additional in-plane magnetic field to break inversion symmetry in conventional SOT switching fundamentally necessitates the development of field-free SOT-driven magnetization switching, especially in perpendicularly magnetized SAFs (p-SAFs) for better scaling [33–37]. The field-free deterministic SOT switching in p-SAFs has predominantly relied on engineered asymmetries (structural or exchange field gradients) [38, 39], in-plane effective field [40, 41], in-plane exchange bias [42], or interlayer Dzyaloshinskii-Moriya interaction (DMI) [43, 44]. Although these methods can break inversion symmetry, their implementation increases the complexity of the device fabrication process, requiring, for instance, the preparation of wedge films or the introduction of additional in-plane anisotropic layers. An alternative approach is to harness the intrinsic symmetry-breaking induced by interfacial DMI at heavy-metal/ferromagnet interfaces [38, 45, 46]. Although DMI breaks spatial inversion symmetry, it also stabilizes homochiral Néel-type domain walls that impose a rotational symmetry constraint on SOT-driven domain wall motion [47, 48], preventing field-free directional domain expansion. Moreover, approaches relying on engineered asymmetry may face challenges in maintaining switching uniformity, reproducibility, and scalability over large device areas, which are critical requirements for practical SOT-MRAM technologies. Thus, achieving field-free deterministic SOT-driven switching in perpendicularly magnetized SAF systems without auxiliary symmetry-breaking operations still remains a fundamental challenge.

In this work, we designed ultra-thin perpendicular SAFs with symmetric ferromagnetic layers, CoFeB (0.6 nm)/W/CoFeB (0.6 nm), with tailored W spacer thicknesses. These SAFs demonstrate field-free deterministic SOT switching at room temperature without any additional engineered structural asymmetries or in-plane magnetic fields. The switching emerges exclusively under antiferromagnetic (AFM) coupling conditions between the two ultrathin magnetic layers, a critical requirement further corroborated by the quantified exchange coupling field (H_{ex}) at different temperatures. The switching chirality (clockwise or counterclockwise) can be reversed by tuning the W spacer thickness and the measurement temperature, suggesting a reversed direction of symmetry-breaking field. Our micromagnetic simulations reveal that the observed deterministic SOT switching in ultra-thin perpendicular SAFs is attributed to a mixed domain wall between Néel and Bloch types, induced by RKKY-type AFM coupling and interfacial DMI, resulting in asymmetric domain wall symmetry breaking. Our work provides an effective approach for field-free deterministic SOT switching using ultra-thin perpendicular SAFs for high-density, low-stray-field, and low-power-consumption SOT-based spintronic devices.

2 | Results and Discussion

2.1 | Field-free Deterministic SOT Switching in SAFs at Room Temperature

Each layer in the samples was fabricated by direct current/radiofrequency (DC/RF) magnetron sputtering sequentially on a Si/SiO_2 substrate. Starting from the bottom layer, the sample structure is composed of SiO_2/MgO (1.48 nm)/CoFeB (0.6 nm)/W (t_W)/CoFeB (0.6 nm)/MgO (1.48 nm)/W (2.48 nm)/Nb (3 nm). High-resolution transmission electron microscopy (HR-TEM) was performed on a sample with t_W = 1.58 nm to determine its atomic structure (Figure 1a). The corresponding elemental mapping is shown in Note S1 (Figure S1), revealing that all layers remained amorphous after rapid thermal annealing. While the two MgO interfaces can be clearly distinguished by atomic contrast, the CoFeB/W interface was not discernible because both metals have amorphous structures [49]. Typically, such an ultrathin CoFeB film exhibits small H_c and weak magnetization [50] due to the magnetic dead layer. More importantly, the perpendicular-magnetized SAF composed of such ultrathin CoFeB has not been realized before. To evaluate the Hall resistance, the samples were patterned into a Hall bar shape using photolithography/ion milling (Figure 1b inset and Figure S2). The Hall resistance (R_{xy} = the Hall voltage (V_H) / electrical current (I_e)) originates mainly from the anomalous Hall effect (AHE) governed by the z-component of the net magnetization. The room-temperature AHE loops of the sample with different thicknesses of W (t_W) all exhibit robust perpendicular magnetic anisotropy (PMA) and relatively large H_c (100 ~ 450 Oe), as demonstrated in the left panels of Figure 1b–f. When H_z is larger than the exchange coupling field (H_{ex}), the stable states correspond to the magnetization of the two CoFeB layers pointing to the +z and −z directions, as displayed in the inset of Figure 1c left panel. As the H_z decreases to a value less than H_{ex}, the magnetization can switch from the parallel state to antiparallel state corresponding to the AFM coupling. The top and bottom CoFeB layers in SAFs with t_W = 2.14, 1.92, 1.58, and 1.36 nm display characteristics of AFM coupling, whereas the t_W = 1.24 nm SAF exhibits FM coupling behavior. These spacer-thickness-dependent AHE loops reflect the classic RKKY-coupled SAF characteristics, demonstrating long-range oscillatory interlayer coupling via hysteresis loop analysis [31, 51, 52].

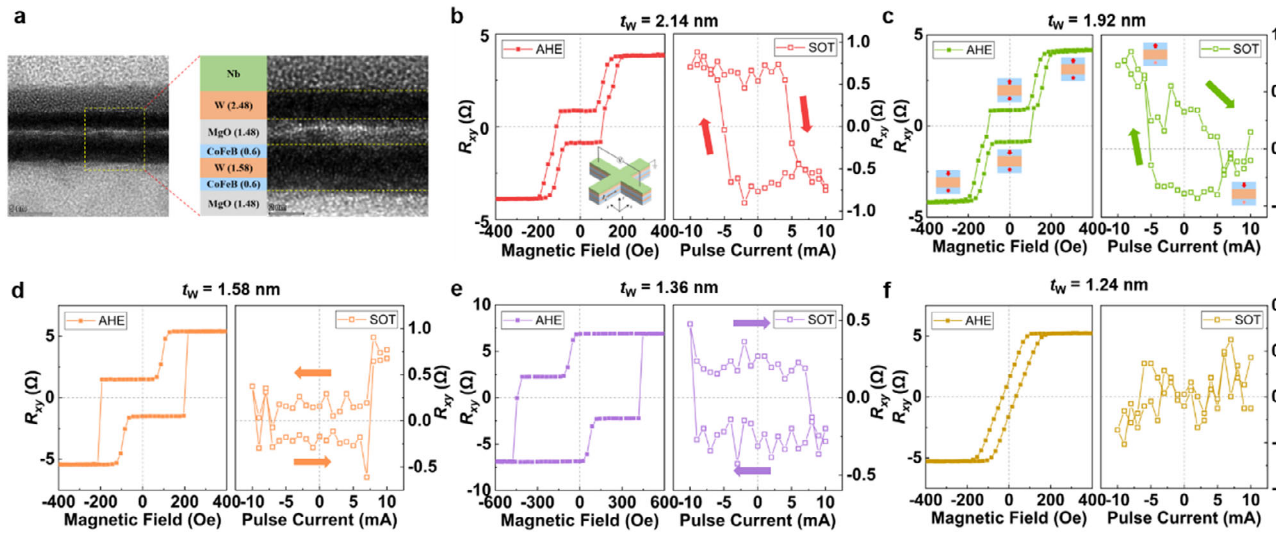

FIGURE 1 | Field-free SOT switching behaviors with the AHE results. (a) Atomic structure of a cross-sectional SAF, MgO/CoFeB/W (1.58 nm)/CoFeB/MgO, by HR-TEM. (b–f) Anomalous Hall loop (left panel) and field-free SOT switching (right panel) of SAFs with different W thicknesses of b) 2.14 nm, c) 1.92 nm, d) 1.58 nm, e) 1.36 nm, and f) 1.24 nm at room temperature. The inset in the left panel of b) is a schematic of the SAF Hall bar for electrical transport measurements. The inset in c) shows a schematic of magnetic moment switching in the SAF Hall bar for AHE loop and SOT switching. The anomalous Hall voltage is measured along the y-axis with currents applied along the x-axis, whereas the magnetic field is swept perpendicular to the device. The Hall bar width is 5 µm. R_{xy} represents the Hall resistance.

In the symmetric SAF structure, we conducted field-free SOT-driven magnetization switching at room temperature. The driving current signal is illustrated in Figure 2a, where successive write current pulses with a duration of 1 ms and a maximum amplitude of 10 mA (current from positive to negative and then back to positive) are injected in the x-axis of the Hall bar, while a sensing current of 100 µA is applied after each pulse to detect the magnetization state via the y-axis R_{xy}. The samples with t_W = 2.14-1.36 nm exhibit field-free SOT switching (Figure 1b–e, right panel), whereas the t_W = 1.24 nm sample shows negligible SOT switching behavior (Figure 1f, right panel), indicating that field-free SOT switching only occurs under AFM coupling. It should be noted that, owing to inherent asymmetries between the two CoFeB/W interfaces and practical limitations on the maximum applicable current density (close to the device breakdown limit), the two CoFeB layers switch with different fractions (inset of the right panel of Figure 1c). Specifically, the switching fractions (at 300 K) are approximately 76% for t_W = 2.14 nm, 41% for t_W = 1.92 nm, and 11% for t_W = 1.58 nm. As a result, although the measured SOT signal appears as partial switching, it originates from deterministic magnetization reversal in both layers. To directly verify the magnetic origin of the field-free SOT switching, magneto-optical Kerr effect microscopy (Truth Instruments KMPL-S) was performed during current sweeping. Progressive and directional domain evolution was observed, with domains nucleating and expanding under one current polarity and reversing along the opposite sequence upon current reversal. This polarity-dependent behavior confirms that the Hall switching loops originate from deterministic current-induced magnetization reversal rather than measurement artifacts (see Note S3 and Figure S3).

To further verify the intrinsic nature of the field-free SOT switching, the in-plane magnetic field (H_x) dependence of the SOT switching was measured on a t_W = 1.92 nm device under H_x = 0, ±20, ±100, ±500, and ±700 Oe. A monotonic decrease of the switching signal with increasing $|H_x|$, together with a field-induced chirality reversal, confirms the intrinsic origin of the field-free SOT switching (see Note S4 and Figure S4). Notably, the field-free SOT switching chirality is clockwise for SAFs with t_W = 2.14, 1.92, and 1.36 nm and counterclockwise for those with t_W = 1.58 nm, indicating that the magnetization switching chirality can be reversed by varying the thickness of the W spacer layer. Meanwhile, the uniformity of field-free SOT switching was verified by measuring six random devices on the same film (t_W = 2.14 nm), all exhibiting consistent switching behavior (see Note S5, Figure S5 and Table S1). Furthermore, a 0.6 nm single-layer CoFeB film does not exhibit field-free SOT switching, where an additional in-plane magnetic field is required to break the symmetry (Note S6 and Figure S6), suggesting that the RKKY interaction plays a crucial role in field-free SOT switching. We also note the concept of interlayer DMI (long-range chiral exchange interaction), which has been identified as an important symmetry-breaking mechanism in SAFs [53–55]. A hallmark of significant interlayer DMI is a unidirectional shift of the switching loops, manifested as finite current and field biases (i.e., offsets along the current and field axes) arising from asymmetric switching thresholds under opposite in-plane fields [44, 53–57]. In our symmetric CoFeB/W/CoFeB structure, SOT switching measurements under in-plane fields of ±20 Oe, ±100 Oe, and ±500 Oe show no detectable asymmetry (Figure S4), indicating that interlayer DMI is not dominant in our system. We therefore attribute the deterministic field-free SOT switching primarily to the interplay between RKKY coupling and

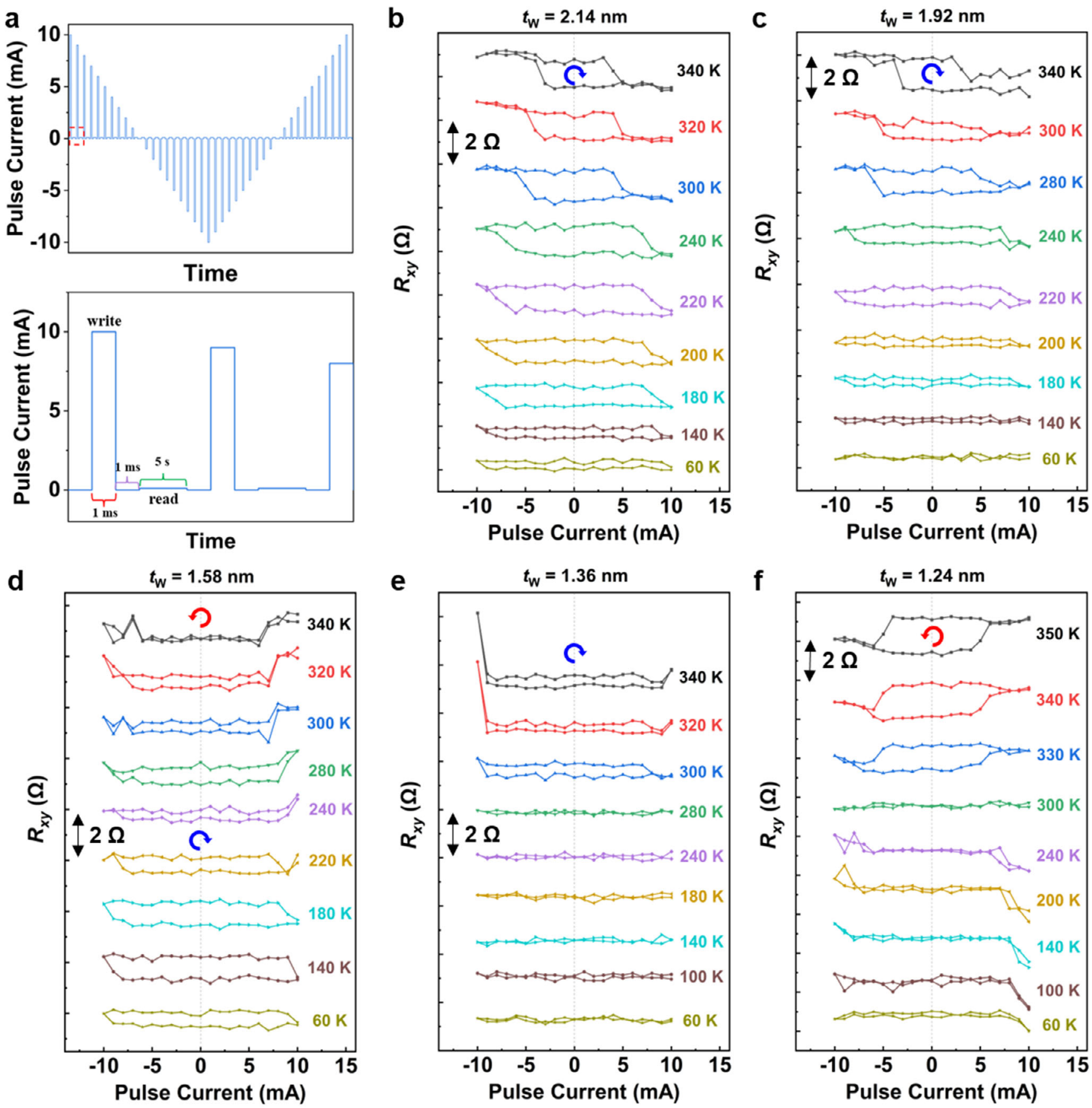

FIGURE 2 | Temperature-dependent field-free SOT switching in MgO/CoFeB (0.6 nm)/W/CoFeB (0.6 nm)/MgO with different W thicknesses. (a) Current pulses for SOT switching measurements. Writing current pulses (±10 mA, 1 ms) were applied to modulate the magnetic state of the CoFeB layers. After each writing pulse, a delay time (1 ms) was set, and then a read current (100 μA, 5 s) was applied to detect the magnetic state of the CoFeB layers by AHE. (b–f) Temperature dependence of field-free SOT switching for the SAFs with W thicknesses of b) 2.14 nm, c) 1.92 nm, d) 1.58 nm, e) 1.36 nm and f) 1.24 nm at different temperatures.

a residual net interfacial DMI arising from unavoidable growth asymmetries.

2.2 | Temperature-Dependent Field-Free SOT Switching With Different W Thicknesses

To delineate a comprehensive picture of the switching behaviors, we systematically conducted field-free SOT switching measurements on SAFs with various spacer thicknesses, t_W = 2.14–1.24 nm, over a temperature range of 60–350 K (corresponding AHE loops are in Note S8, Figures S8–S11). Following the same measurement method (Figure 2a), in the sample with t_W = 2.14 nm (Figure 2b), the critical SOT switching current decreases monotonically with increasing temperature, a behavior originating from the thermal-fluctuation-induced reduction of PMA, while it exhibits a consistent clockwise switching chirality in the entire temperature range. The sample with t_W = 1.92 nm (Figure 2c) exhibits the same clockwise field-free SOT switching characteristics.

Intriguingly, reducing the W thickness to 1.58 nm (Figure 2d) reveals a distinct temperature-dependent field-free SOT switching behavior. While field-free SOT switching persists over 60–320 K, a notable switching chirality reversal occurs at ≈240 K, with clockwise switching below and counterclockwise above this temperature. This temperature-tunable switching of chirality has not been previously reported [39, 41]. The SOT switching loop vanished at 340 K due to strong thermal agitation. The temperature dependence of the SOT switching, as determined from the AHE loops (Figure S9), may reflect the presence of interlayer exchange coupling (IEC). In addition, the reproducibility of field-free SOT switching was confirmed by six consecutive measurements on an additional $t_W = 1.58$ nm device at 300 K, showing consistent counterclockwise switching behavior (see Note S7 and Figure S7).

When the W thickness decreases to 1.36 nm (Figure 2e), SOT switching is absent below 280 K. A minor but robust clockwise switching chirality emerges at 300 K, with a small switching ratio of ~4% that persists at 340 K. This is corroborated by the AHE loop (Figure S10), which confirms the lack of field-free SOT switching in the FM coupled state. With a further reduction in W thickness to 1.24 nm, SOT switching is absent at 60–300 K, where the behavior is similar to that of the sample with $t_W = 1.36$ nm, in which no SOT switching occurs under FM coupling (Figure S11). This confirms that field-free SOT switching in the SAF system requires AFM coupling exclusively. The 300 K field-free SOT switching data for the $t_W = 1.24$ nm sample shown in Figure 1f are identical to the 300 K loop presented in Figure 2f. The apparent difference in signal-to-noise ratio arises from the different vertical scales used in the two panels. Remarkably, a counterclockwise SOT switching emerges near 330 K, with a higher switching ratio than that of the sample with $t_W = 1.36$ nm, underscoring the role of W thickness in modulating thermal stability and switching chirality. This thickness-mediated chirality control may arise from the interplay between RKKY coupling and a net chiral effective field (e.g., due to asymmetric interfacial DMI or a weak interlayer DMI).

We propose that the temperature dependence of field-free SOT switching is governed by the following mechanism: thermal weakening of PMA directly reduces the critical switching current and leads to the disappearance of switching at elevated temperatures. More importantly, the observed reversal of switching chirality indicates that the net chiral-symmetry-breaking effective field changes sign with temperature. In the SAF with symmetric interfaces, the DMI contributions from the top and bottom CoFeB/W interfaces may compete. When the spacer thickness (e.g., $t_W = 1.58$ nm) lies near a critical region of the RKKY oscillation period, variations in temperature can significantly modulate the combined effect of the two interfacial DMI terms by altering the IEC strength or inducing noncollinear magnetic configurations. Once this net effective field reverses beyond a critical temperature, the chirality of the stabilized domain walls also reverses, ultimately leading to the inversion of the SOT-driven magnetization switching chirality.

The critical switching current density (J_c), a key metric for SOT switching behavior, was derived using the parallel circuit model (Note S9 and Figure S12). Here, J_c is defined as the minimum current density flowing through the W spacer required to induce

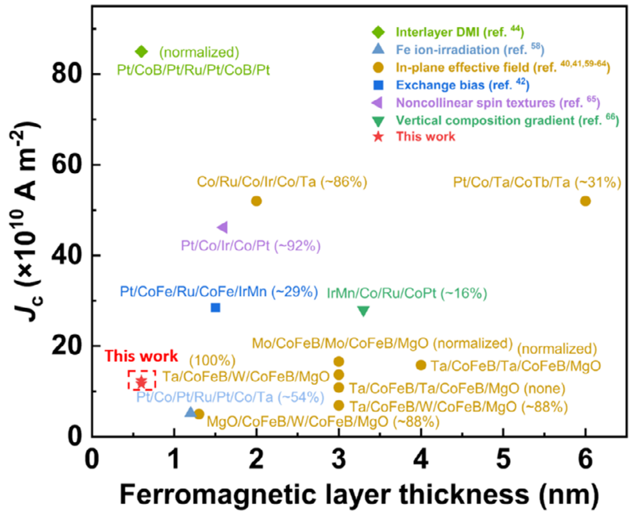

FIGURE 3 | A summary of critical switching current density J_c of field-free SOT switching at 300 K for conventional SAFs. Comparison of J_c in this work (red-dotted box) with previously reported conventional SAFs with field-free SOT switching. The percentages in the figure represent the field-free SOT switching ratio of the literature, where "normalized" indicates that the ordinate of the AHE or SOT curve of the literature has been normalized, and "none" indicates that the AHE curve is not displayed.

a complete switch in the SOT switching loop. Figure 3 compares the field-free SOT critical switching current J_c observed from SAFs with different ferromagnetic layer thicknesses. Data points are classified by color and shape according to the mechanism enabling field-free SOT switching, including interlayer DMI [44], ion irradiation [58], in-plane effective field [40, 41, 59–64], exchange bias [42], noncollinear spin textures [65], and vertical composition gradient [66]. Our SAF structure has achieved a J_c of 7.82×10^{10} A m^{-2}, an order of magnitude lower than that of conventional SAFs with similar ferromagnetic thicknesses, and is comparable to the lowest reported values in various SAF systems. Meanwhile, while maintaining a low J_c, the thermal stability factor (Δ) of the device is estimated to be $\Delta \approx 20$ at room temperature (see Note S10, Figure S13 and Table S2), indicating a reasonable balance between switching efficiency and thermal stability. It should be noted that most previously reported field-free SOT switching in SAFs, including our present work (≈76% and ≈41%), exhibit partial switching rather than complete magnetization switching. Within this context, we have compared our J_c values with those reported in the literature, labeling their respective switching ratios when provided (Figure 3). A complete summary of the field-free SOT switching ratios for all SAF devices investigated in this work is provided (see Note S10, Table S3). Notably, this study demonstrates field-free deterministic SOT switching in a SAF incorporating ultra-thin (0.6 nm) magnetic CoFeB layers. A key advantage of such thin layers is their ability to mitigate electrostatic screening effects [67–69], which enables efficient magnetization manipulation via external electric fields, such as nonvolatile ferroelectric polarization. Physically, properties such as interfacial electronic structure [70], DMI [71], magnetic domain walls [72], and magnetic skyrmions [73] can differ markedly from those in thicker films. From an application perspective, such layers exhibit low magnetization and enable reduced switching voltages [74–77]. Although ultrathin CoFeB

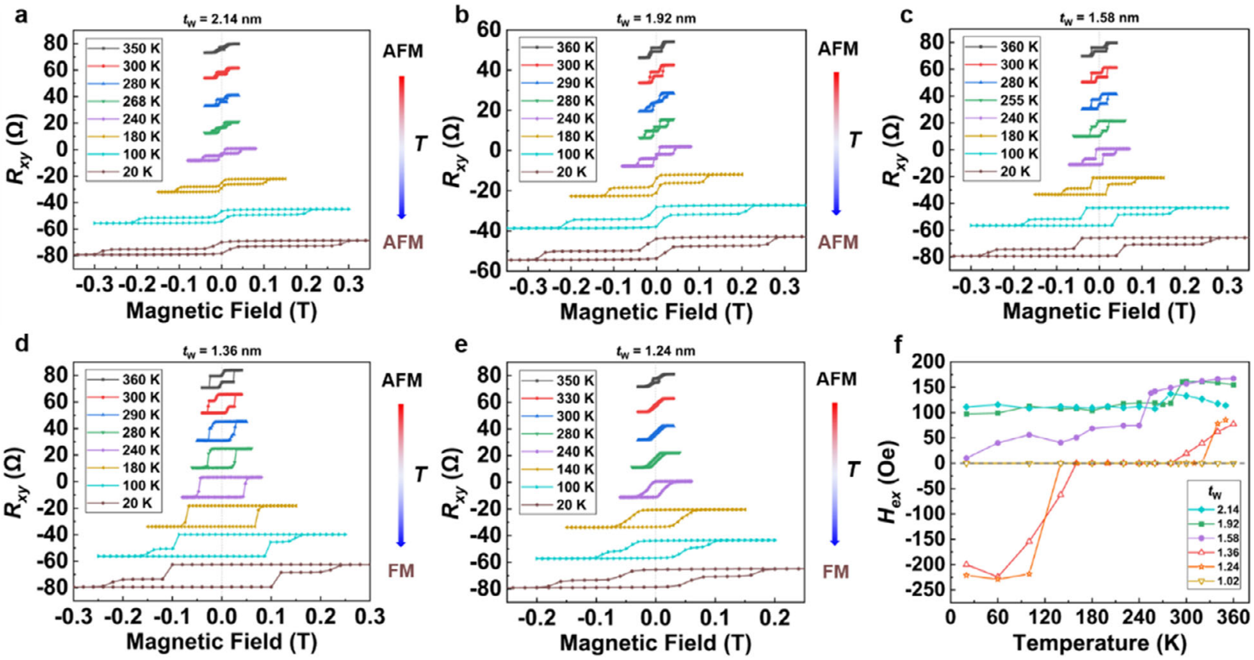

FIGURE 4 | Temperature-dependent AHE behaviors of MgO/CoFeB (0.6 nm)/W/CoFeB (0.6 nm)/MgO with different W thicknesses. (a–e) R_{xy} of the SAFs with W thicknesses of a) 2.14 nm, b) 1.92 nm, c) 1.58 nm, d) 1.36 nm and e) 1.24 nm as a function of the perpendicular magnetic field at temperatures ranging from 20 to 360 K. f) Extracted H_{ex} of the SAFs from a–e).

layers typically exhibit enhanced magnetic damping due to interfacial spin pumping and two-magnon scattering [78], the reduced total magnetic moment in these layers can lower the switching energy barrier, thereby enabling effective low-power SOT switching.

2.3 | Temperature-Dependent Interlayer Exchange Coupling

Given that field-free deterministic SOT switching occurs only under AFM coupling across a broad temperature range, understanding the temperature dependence of IEC is essential to elucidate the SOT switching mechanism. Systematic AHE behaviors were performed on samples with $t_W = 1.02$–2.14 nm at 20–360 K (Figure 4a–e, Note S12 and Figures S15, S16). From these loops, six critical parameters were extracted: H_{ex}, coercivity (H_c), remanent R_{xy} ($R_{xy\text{-}r}$), saturation field (H_{sat}), saturation R_{xy} ($R_{xy\text{-}s}$), and squareness ($R_{xy\text{-}r}/R_{xy\text{-}s}$), to establish quantitative correlations between magnetic switching and thermal effects (Figure 4f, Note S13), where the H_{ex} was determined via minor-loop analysis (Note S11 and Figure S14). Additionally, temperature-dependent AHE behavior of a single 0.6 nm CoFeB layer confirms ferromagnetic order throughout the temperature range of 20–350 K (Note S14 and Figure S19).

In the sample with t_W = 2.14 nm, the AHE loops exhibit a transition near 220 and 268 K (Figure 4a and Figure S16a) from tris-loop to double-loop. Despite these changes, AFM coupling is maintained, as indicated by consistently positive H_{ex} (Figure 4f). These transitions are more clearly reflected in abrupt changes in H_c and $R_{xy\text{-}r}$ (Figure S17), arising from competing energy contributions involving exchange, anisotropy, and Zeeman interactions [79, 80]. Similar AFM-coupled behavior is observed in the sample with $t_W = 1.92$ nm, with transition temperatures near 220 and 290 K (Figure 4b and Figure S16b), consistent with its field-free SOT switching characteristics. The sample with $t_W = 1.58$ nm exhibits an unstable AHE loop evolution near 255 K while retaining AFM coupling (Figure 4c). Located near an RKKY oscillation node, its IEC is highly sensitive to temperature, resulting in a metastable region (t_W = ≈1.58 nm) (Figure 4f). Unlike the continuous evolution in SAFs with thicker t_W, a reversal of the net chiral effective field may emerge due to the extreme sensitivity of the interlayer exchange coupling near the RKKY oscillation node under thermal perturbations, leading to a change in the preferred Néel domain-wall chirality and consequently in the observed SOT switching direction.

When t_W is reduced to 1.36 nm, the AHE loop evolves continuously with transitions near 160 and 280 K (Figure 4d and Figure S16d). Above 280 K, $H_{ex} > 0$ indicates RKKY-type AFM coupling. Between 160–280 K, H_{ex} = 0 (single-loop behavior) suggests the probable emergence of pinhole-mediated FM coupling [81]. Below 160 K, $H_{ex} < 0$ suggests RKKY-type FM coupling. The sample with $t_W = 1.24$ nm shows similar coupling behavior with transitions shifted to ≈140 and 320 K. More slanted hysteresis loops were observed over a wider temperature range, indicating higher pinhole density. The pinhole density at t_W = 1.36 nm should be relatively low, as evidenced by robust PMA. Thus, even minimal pinholes can significantly influence coupling in such an ultrathin structure.

For t_W = 1.02 nm, a slanted single-loop hysteresis persists in the entire temperature range, indicating strong FM coupling. A comprehensive phase diagram was constructed to delineate the three coupling regimes: RKKY-type AFM, RKKY-type FM, and pinhole-induced FM, as a function of t_W and temperature (Figure S18d). The samples with t_W ≥ 1.58 nm retain RKKY

AFM coupling, while thinner spacer layers exhibit temperature-dependent competition among various coupling mechanisms. Crucially, these findings confirm that ferromagnetic coupling, regardless of origin, inhibits field-free SOT switching.

2.4 | Spin Dynamics and Domain Evolution of CoFeB/W/CoFeB SAF

To gain deeper insights into the field-free SOT switching mechanism in ultrathin SAF structures, micromagnetic simulations were performed to model the switching dynamics of magnetic domains in the two CoFeB layers. The simulations solved the Landau-Lifshitz-Gilbert equation using Mumax3 in a $360 \times 50 \times 1.2\ nm^3$ region. The nonmagnetic spacer layer is not explicitly modeled, but is incorporated through its effective RKKY interaction. We first performed systematic micromagnetic simulations by sweeping the RKKY coupling strength and the interfacial DMI constant over experimentally relevant ranges (see Methods and Note S15). The results show that deterministic field-free SOT switching occurs only for AFM RKKY coupling ($J < 0$) and within a finite window of DMI values, whereas no switching is observed for FM coupling, in agreement with experiments (Figure S20).

Based on this parameter mapping, we then focus on a representative set of parameters that yields complete magnetization reversal, with the RKKY coupling energy set to $J = \pm 0.004$ J m^{-2} and the interfacial DMI constant of the bottom CoFeB layer set to $D_b = -8 \times 10^{-4}$ J m^{-2}. The driving current is illustrated in Figure 5a. Under AFM coupling conditions, initial magnetizations of the top ($+\mathbf{m}_z$) and bottom ($-\mathbf{m}_z$) CoFeB layers are set antiparallel. Note that the plotted m_z is the z-component of the normalized magnetization vector and reflects only the magnetization direction. The AHE signal is proportional to the effective perpendicular magnetization. Because the two CoFeB layers have unequal effective perpendicular magnetic moment densities, their opposite switching does not fully cancel, resulting in a finite signal. While applying a positive current pulse, the magnetic moments of both layers tilt predominantly along the x-direction at approximately 0.2 ns (Figure 5b and Figure S21a). The moments underwent nonuniform oscillations, spontaneously forming domain walls before relaxing into opposite states via domain wall motion within 0.2 ns, a nearly symmetric process for the $\mathbf{m}_y$ and $\mathbf{m}_z$ components between layers (Figure 5d,e and Figure S22a, b). Snapshots of the magnetic moments in the bottom CoFeB layer revealed that current injection, combined with RKKY and DMI, led to a dynamic noncollinear spin texture within 0.03 ns, identified as a hybrid Néel-Bloch domain wall (Figure S23b).

To clarify the microscopic origin of the deterministic field-free switching, we analyze the symmetry of the domain wall configuration under SOT. In a pure Néel-type domain wall, two configurations with opposite chirality are degenerate (Figure S23a), and under a given current-induced spin polarization, they experience SOT-driven forces of equal magnitude but opposite direction, resulting in no preferred direction for domain wall motion [48, 82, 83]. Importantly, the presence of a Néel-Bloch mixed domain wall (Figure S23b) does not by itself break this symmetry. In a perfectly symmetric SAF, the domain walls in the two layers remain antisymmetric due to AFM coupling, and the in-plane magnetization components are fully compensated, leading to a complete cancellation of the SOT-induced forces even when both Néel and Bloch components are present. In our system, however, the two CoFeB layers are not strictly equivalent due to interfacial asymmetry (e.g., MgO/CoFeB versus W/CoFeB), which leads to different interfacial DMI contributions and magnetic parameters. As shown in Figure 5f,g, when combined with RKKY-mediated AFM coupling, the red dashed box compares the magnetic domain structures of the upper and lower CoFeB layers at the same position under the same pulse current time, showing asymmetric Néel-Bloch mixed domain walls. As a result, the in-plane magnetization components of the two domain walls do not fully compensate, resulting in incomplete cancellation of the SOT-driven forces. This gives rise to a finite net driving force on the coupled domain wall, which can be equivalently viewed as an effective in-plane field that breaks the chirality symmetry and selects a preferred direction for domain wall motion. This interpretation is further supported by the MOKE microscopy measurements (Figure S3), where under zero external magnetic field the magnetization reversal proceeds through reproducible directional domain evolution: one side of the Hall bar switches first, followed by domain expansion across the device, while the propagation sequence reverses under opposite current polarity. Such polarity-dependent domain-wall motion is consistent with the existence of a finite uncompensated driving force. Therefore, the deterministic field-free switching originates from the asymmetry of the coupled domain wall structure.

This structure provided a nonzero driving force, enabling deterministic magnetization switching via the propagation of strip-domain walls (before 0.19 ns) and wave-curved walls (after 0.25 ns). Although the domain structure continuously evolved, the hybrid domain walls remained throughout, exhibiting components along all three axes. After the current pulse terminates at 5 ns, the system relaxed toward a uniform state within 0.2 ns, showing sub-nanosecond relaxation dynamics (Figure 5e). A similar magnetization switching process occurred in the top CoFeB layer (Figure S22). In contrast, under FM coupling (e.g., both layers initialized downward), the applied current pulse only resulted in damped precession of the magnetic moments without deterministic magnetization switching (Figure 5c, Figures S21b and S24). No sustained noncollinear spin texture or chiral domain wall was found in this case to break the inversion symmetry.

It is well known that DMI at heavy-metal/ferromagnet interfaces stabilizes homochiral Néel walls [45], whose configuration yields a negligible net driving force under SOT, preventing deterministic magnetization switching without an in-plane field. In contrast to prior observations in both FM-coupled (CoNi/Ir/CoNi [84]) and AFM-coupled (Co/Ni/Co [65]) SAFs, our study demonstrates that RKKY-mediated AFM coupling, synergizing with DMI, stabilizes hybrid Néel-Bloch domain walls, and the domain walls of the upper and lower ferromagnetic layers are asymmetric. This distinct symmetry-breaking configuration is the key to achieving robust field-free SOT switching. Furthermore, the IEC, which governs magnetic interactions and spin dynamics, exhibits strong thickness- and temperature-dependent behavior in the spacer layer. Sub-nanometer thickness variations can shift the IEC between AFM and FM regimes, thereby mediating DMI reconfiguration to achieve deterministic field-free switching.

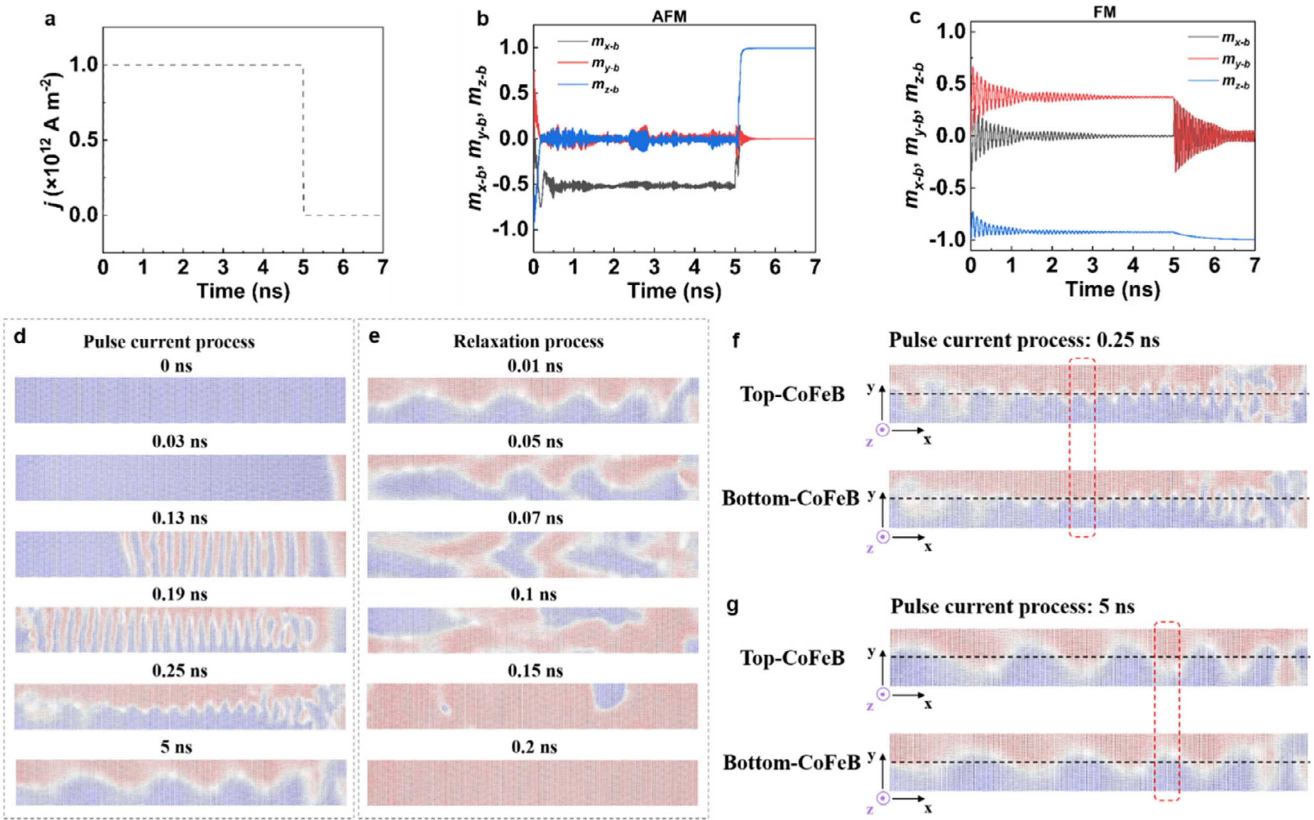

FIGURE 5 | Micromagnetic simulation. (a) Current pulse applied to W spacer for SOT switching: 5 ns pulse with a current density of 1×10^{12} A m^{-2} and a 2 ns relaxation process. (b, c) Switching dynamics of magnetization m driven by current pulses with b) AFM coupling and c) FM coupling for the bottom-CoFeB. The $m_{x\text{-}b}$, $m_{y\text{-}b}$, and $m_{z\text{-}b}$ represent components of the normalized magnetization vector in the x, y, and z directions of the bottom CoFeB layer, ranging from −1 to +1. (d, e) The snapshots of the magnetic domain structure in the x-y plane during the d) pulse current process and e) relaxation process, respectively. The values of m_z are defined by red (+m_z) and blue (-m_z) colors, where darker colors indicate larger magnitudes of the m_z component. White areas represent mixed domain walls with in-plane components. (f, g) The snapshots of the magnetic domain structure in the x-y plane at f) 0.25 ns and g) 5 ns, the pulse current process for the top-CoFeB and bottom-CoFeB layers. The red dotted lines enclose the magnetic domains at the same positions on the top and bottom layers.

3 | Conclusions

In summary, this work demonstrates field-free deterministic SOT switching in ultrathin perpendicular CoFeB/W/CoFeB SAFs at room temperature via controlled W spacer thickness, eliminating the need for complex structural asymmetry or external magnetic fields. Systematic experiments establish that field-free SOT switching occurs exclusively under AFM coupling, with chirality determined by the effective field sign in the system. Temperature-dependent H_{ex} analysis quantitatively links AFM coupling strength to SOT switching characteristics across spacer thicknesses. Micromagnetic simulations reveal that RKKY-mediated AFM coupling, together with DMI, stabilizes Néel-Bloch mixed domain walls. The asymmetric mixed-domain walls in the top and bottom CoFeB layers break symmetry, enabling deterministic switching. By mapping thickness-temperature phase diagrams and clarifying mechanisms for chirality control, this study offers a general strategy for designing high-density SOT-MRAM with low stray fields and reduced power consumption.

4 | Experimental Section

4.1 | Sample Growth and Characterization

All samples were deposited by magnetron sputtering at room temperature onto thermally oxidized Si (100) substrates coated with 300 nm of SiO_2. The base pressure was better than 3.8×10^{-5} mTorr. In the heterostructures, the bottom 1.48-nm-thick MgO layer served as a buffer to improve film adhesion, and the top 2.48-nm-thick W layer and 3-nm-thick Nb layer served as a capping layer to prevent sample oxidation in air. The deposition rate of CoFeB using direct current (dc) sputtering was 0.166 Å s^{-1}, and the deposition rate of MgO using radio frequency (rf) sputtering was 0.0489 Å s^{-1}, at an Ar pressure of 1.5 and 2 mTorr, respectively. The deposition rates of W and Nb were 0.102 Å s^{-1} (dc, 1.2-mTorr Ar) and 0.12 Å s^{-1} (rf, 1.7-mTorr Ar), respectively, which were calibrated by ellipsometer and atomic force microscopy. After deposition, multilayer structures were rapidly annealed at 300°C for 2 min in a N_2 atmosphere. Microstructural characterization was conducted via HR-TEM using cross-sectional specimens prepared by focused ion beam milling.

4.2 | Device Fabrication

The magnetic films were patterned into Hall bar devices with a channel width of 5 μm and a length of 36 μm using ultraviolet lithography and Ar-ion beam etching. Then, contact pads of Ti (15 nm)/Au (45 nm) layers were deposited by electron-beam evaporation and lift-off, serving as electrodes to reduce contact resistance.

4.3 | Electrical Measurements

Temperature-dependent AHE and SOT switching measurements were carried out in a magnetic probe station (Lake Shore CRX-VF) from 20 to 360 K. For the AHE loops, an out-of-plane magnetic field was scanned with a 100 μA applied current, using a Keithley 2182A nanovoltmeter and a Keithley 6221 current source. The SOT switching was characterized by injecting a series of 1-ms writing current pulses (±10 mA range, 1 mA step) into the longitudinal channel. After a 1-ms delay, the magnetization state was read by applying a 100 μA sensing current for 5 s, with the final Hall resistance taken as the median of 50 consecutive readings.

4.4 | Micromagnetic Simulation

Micromagnetic simulations were performed using the Mumax3 software package to investigate magnetization dynamics during the switching process. These simulations were governed by the LLG equation, which was extended to include SOT terms to model the influence of spin-orbit interactions. The simulated structure comprised a double-layer CoFeB film, with each layer having a uniform thickness of 0.6 nm, resulting in a total thickness of 1.2 nm. The computational domain, representing the entire simulated structure, had dimensions of 360 nm in length, 50 nm in width, and 1.2 nm in height. This domain was discretized into a cuboid mesh for the simulation. To focus exclusively on the intrinsic magnetization behavior driven by SOT, all simulations were performed at absolute zero (0 K) and in the absence of an external magnetic field. The simulated parameters were following CoFeB/W/CoFeB system: top-CoFeB saturation magnetization $M_{s\text{-}t} = 1.078 \times 10^6$ A m^{-1}, bottom-CoFeB saturation magnetization $M_{s\text{-}b} = 0.843 \times 10^6$ A m^{-1} according to experiments, exchange stiffness $A = 1 \times 10^{-11}$ J m^{-1} (Ref. [85]), uniaxial anisotropy constant $K_u = 8 \times 10^5$ J m^{-3} according to experiments and literature (Ref. [49, 86]) and spin Hall angle θ_{SH} = -0.3 (Ref. [32]). The interfacial DMI constant of bottom-CoFeB was set to $D_b = [-1.0 \times 10^{-3}, -0.4 \times 10^{-3}]$ J m^{-2} (Ref. [86–88]), the step was 0.1×10^{-3}, and the interfacial DMI constant of top-CoFeB was set to $D_t = 1.2\, D_b$. The RKKY energy was set to $J = [-1.0 \times 10^{-2}, 1 \times 10^{-2}]$ J m^{-2} according to experiments and literature (Ref. [49]), step was 2×10^{-3}. The simulated current density was $j = 1 \times 10^{12}$ A m^{-2}. The pulse current time was 5 ns, and the relaxation time was 2 ns.

Acknowledgements

This work was financially supported by the National Key R&D Program of China (Grants No. 2021YFA1202200).

Conflicts of Interest

The authors declare no conflicts of interest.

Data Availability Statement

The data that support the findings of this study are available from the corresponding author upon reasonable request.

References

1. K. L. Wang, J. G. Alzate, and P. K. Amiri, "Low-power Non-volatile Spintronic Memory: STT-RAM and Beyond," *Journal of Physics D: Applied Physics* 46 (2013): 074003, https://doi.org/10.1088/0022-3727/46/7/074003.

2. A. Hirohata, H. Sukegawa, H. Yanagihara, et al., "Roadmap for Emerging Materials for Spintronic Device Applications," *IEEE Transactions on Magnetics* 51 (2015): 1–11, https://doi.org/10.1109/TMAG.2015.2457393.

3. Z. Guo, J. Yin, Y. Bai, et al., "Spintronics for Energy- Efficient Computing: An Overview and Outlook," *Proceedings of the IEEE* 109 (2021): 1398–1417, https://doi.org/10.1109/JPROC.2021.3084997.

4. I. M. Miron, K. Garello, G. Gaudin, et al., "Perpendicular Switching of a Single Ferromagnetic Layer Induced by in-plane Current Injection," *Nature* 476 (2011): 189–193, https://doi.org/10.1038/nature10309.

5. L. Liu, C. F. Pai, Y. Li, H. W. Tseng, D. C. Ralph, and R. A. Buhrman, "Spin-Torque Switching with the Giant Spin Hall Effect of Tantalum," *Science* 336 (2012): 555–558, https://doi.org/10.1126/science.1218197.

6. Q. Shao, P. Li, L. Liu, et al., "Roadmap of Spin–Orbit Torques," *IEEE Transactions on Magnetics* 57 (2021): 1–39, https://doi.org/10.1109/TMAG.2021.3078583.

7. X. Han, X. Wang, C. Wan, G. Yu, and X. Lv, "Spin-orbit Torques: Materials, Physics, and Devices," *Applied Physics Letters* 118 (2021): 120502, https://doi.org/10.1063/5.0039147.

8. K. C. Chun, H. Zhao, J. D. Harms, T. H. Kim, J. P. Wang, and C. H. Kim, "A Scaling Roadmap and Performance Evaluation of in-Plane and Perpendicular MTJ Based STT-MRAMs for High-Density Cache Memory," *IEEE Journal of Solid-State Circuits* 48 (2013): 598–610, https://doi.org/10.1109/JSSC.2012.2224256.

9. S. Amara-Dababi, R. C. Sousa, M. Chshiev, et al., "Charge Trapping-detrapping Mechanism of Barrier Breakdown in MgO Magnetic Tunnel Junctions," *Applied Physics Letters* 99 (2011): 083501, https://doi.org/10.1063/1.3615654.

10. K. S. Lee, S. W. Lee, B. C. Min, and K. J. Lee, "Threshold Current for Switching of a Perpendicular Magnetic Layer Induced by Spin Hall Effect," *Applied Physics Letters* 102 (2013): 112410, https://doi.org/10.1063/1.4798288.

11. K. Roy, "Ultra-low-energy Computing Paradigm Using Giant Spin Hall Devices," *Journal of Physics D: Applied Physics* 47 (2014): 422001, https://doi.org/10.1088/0022-3727/47/42/422001.

12. Q. Hao and G. Xiao, "Giant Spin Hall Effect and Switching Induced by Spin-Transfer Torque in a W/$Co_{40}Fe_{40}B_{20}$/MgO Structure with Perpendicular Magnetic Anisotropy," *Physical Review Applied* 3 (2015): 034009, https://doi.org/10.1103/PhysRevApplied.3.034009.

13. K. Garello, C. O. Avci, I. M. Miron, et al., "Ultrafast Magnetization Switching by Spin-orbit Torques," *Applied Physics Letters* 105 (2014): 212402, https://doi.org/10.1063/1.4902443.

14. K. Ando, S. Takahashi, K. Harii, et al., "Electric Manipulation of Spin Relaxation Using the Spin Hall Effect," *Physical Review Letters* 101 (2008): 036601, https://doi.org/10.1103/PhysRevLett.101.036601.

15. L. Liu, T. Moriyama, D. C. Ralph, and R. A. Buhrman, "Spin-Torque Ferromagnetic Resonance Induced by the Spin Hall Effect," *Physical Review Letters* 106 (2011): 036601, https://doi.org/10.1103/PhysRevLett.106.036601.

16. T. Jungwirth, J. Wunderlich, and K. Olejnik, "Spin Hall Effect Devices," *Nature Materials* 11 (2012): 382–390, https://doi.org/10.1038/nmat3279.

17. A. Manchon and S. Zhang, "Theory of Nonequilibrium Intrinsic Spin Torque in a Single Nanomagnet," *Physical Review B* 78 (2008): 212405, https://doi.org/10.1103/PhysRevB.78.212405.

18. P. M. Haney, H. W. Lee, K. J. Lee, A. Manchon, and M. D. Stiles, "Current Induced Torques and Interfacial Spin-orbit Coupling: Semiclassical Modeling," *Physical Review B* 87 (2013): 174411, https://doi.org/10.1103/PhysRevB.87.174411.

19. Q. Shao, G. Yu, Y. W. Lan, et al., "Strong Rashba-Edelstein Effect-Induced Spin–Orbit Torques in Monolayer Transition Metal Dichalcogenide/Ferromagnet Bilayers," *Nano Letters* 16 (2016): 7514–7520, https://doi.org/10.1021/acs.nanolett.6b03300.

20. Y. Du, H. Gamou, S. Takahashi, S. Karube, M. Kohda, and J. Nitta, "Disentanglement of Spin-Orbit Torques in Pt/Co Bilayers with the Presence of Spin Hall Effect and Rashba-Edelstein Effect," *Physical Review Applied* 13 (2020): 054014, https://doi.org/10.1103/PhysRevApplied.13.054014.

21. C. Yoshida, T. Takenaga, Y. Iba, et al., "Enhanced Thermal Stability in Perpendicular Top-Pinned Magnetic Tunnel Junction with Synthetic Antiferromagnetic Free Layers," *IEEE Transactions on Magnetics* 49 (2013): 4363–4366, https://doi.org/10.1109/TMAG.2013.2248350.

22. S. H. Yang, K. S. Ryu, and S. Parkin, "Domain-wall Velocities of up to 750 Ms^{-1} Driven by Exchange-coupling Torque in Synthetic Antiferromagnets," *Nature Nanotechnology* 10 (2015): 221–226, https://doi.org/10.1038/nnano.2014.324.

23. R. A. Duine, K. J. Lee, S. S. P. Parkin, and M. D. Stiles, "Synthetic Antiferromagnetic Spintronics," *Nature Physics* 14 (2018): 217–219, https://doi.org/10.1038/s41567-018-0050-y.

24. B. R. Zink, D. Zhang, H. Li, et al., "Ultralow Current Switching of Synthetic-Antiferromagnetic Magnetic Tunnel Junctions via Electric-Field Assisted by Spin–Orbit Torque," *Advanced Electronic Materials* 8 (2022): 2200382, https://doi.org/10.1002/aelm.202200382.

25. D. Lyu, D. Zhang, D. B. Gopman, Y. Lv, O. J. Benally, and J.-P. Wang, "Ferromagnetic Resonance and Magnetization Switching Characteristics of Perpendicular Magnetic Tunnel Junctions with Synthetic Antiferromagnetic Free Layers," *Applied Physics Letters* 120 (2022): 012404, https://doi.org/10.1063/5.0075043.

26. Y. Guan, X. Zhou, F. Li, T. Ma, S. H. Yang, and S. S. P. Parkin, "Ionitronic Manipulation of Current-induced Domain Wall Motion in Synthetic Antiferromagnets," *Nature Communications* 12 (2021): 5002, https://doi.org/10.1038/s41467-021-25292-1.

27. P. He, X. Qiu, V. L. Zhang, Y. Wu, M. H. Kuok, and H. Yang, "Continuous Tuning of the Magnitude and Direction of Spin-Orbit Torque Using Bilayer Heavy Metals," *Advanced Electronic Materials* 2 (2016): 1600210, https://doi.org/10.1002/aelm.201600210.

28. P. Sethi, S. Krishnia, S. H. Li, and W. S. Lew, "Modulation of Spin-orbit Torque Efficiency by Thickness Control of Heavy Metal Layers in Co/Pt Multilayers," *Journal of Magnetism and Magnetic Materials* 426 (2017): 497–503, https://doi.org/10.1016/j.jmmm.2016.11.130.

29. K. D. Belashchenko, A. A. Kovalev, and M. van Schilfgaarde, "Interfacial Contributions to Spin-orbit Torque and Magnetoresistance in Ferromagnet/Heavy-metal Bilayers," *Physical Review B* 101 (2020): 020407, https://doi.org/10.1103/PhysRevB.101.020407.

30. N. H. D. Khang, Y. Ueda, and P. N. Hai, "A Conductive Topological Insulator with Large Spin Hall Effect for Ultralow Power Spin–orbit Torque Switching," *Nature Materials* 17 (2018): 808–813, https://doi.org/10.1038/s41563-018-0137-y.

31. S. S. Parkin, "Systematic Variation of the Strength and Oscillation Period of Indirect Magnetic Exchange Coupling through the 3 D , 4 D , and 5 D Transition Metals," *Physical Review Letters* 67 (1991): 3598–3601, https://doi.org/10.1103/PhysRevLett.67.3598.

32. C. F. Pai, L. Liu, Y. Li, H. W. Tseng, D. C. Ralph, and R. A. Buhrman, "Spin Transfer Torque Devices Utilizing the Giant Spin Hall Effect of Tungsten," *Applied Physics Letters* 101 (2012): 122404, https://doi.org/10.1063/1.4753947.

33. G. Y. Shi, C. H. Wan, Y. S. Chang, et al., "Spin-orbit Torque in MgO/CoFeB/Ta/CoFeB/MgO Symmetric Structure with Interlayer Antiferromagnetic Coupling," *Physical Review B* 95 (2017): 104435, https://doi.org/10.1103/PhysRevB.95.104435.

34. Q. Ma, Y. Li, Y.-S. Choi, W. C. Chen, S. J. Han, and C. L. Chien, "Spin Orbit Torque Switching of Synthetic Co/Ir/Co Trilayers with Perpendicular Anisotropy and Tunable Interlayer Coupling," *Applied Physics Letters* 117 (2020): 172403, https://doi.org/10.1063/5.0024724.

35. P. X. Zhang, L. Y. Liao, G. Y. Shi, et al., "Spin-orbit Torque in a Completely Compensated Synthetic Antiferromagnet," *Physical Review B* 97 (2018): 214403, https://doi.org/10.1103/PhysRevB.97.214403.

36. Y. Saito, S. Ikeda, and T. Endoh, "Enhancement of Current to Spin-current Conversion and Spin Torque Efficiencies in a Synthetic Antiferromagnetic Layer Based on a Pt/Ir/Pt Spacer Layer," *Physical Review B* 105 (2022): 054421, https://doi.org/10.1103/PhysRevB.105.054421.

37. R. Q. Zhang, G. Y. Shi, J. Su, et al., "Tunable Spin–orbit Torque Switching in Antiferromagnetically Coupled CoFeB/Ta/CoFeB," *Applied Physics Letters* 117 (2020): 212403, https://doi.org/10.1063/5.0031415.

38. R. Chen, Q. Cui, L. Liao, et al., "Reducing Dzyaloshinskii-Moriya Interaction and Field-free Spin-orbit Torque Switching in Synthetic Antiferromagnets," *Nature Communications* 12 (2021): 3113, https://doi.org/10.1038/s41467-021-23414-3.

39. H. Fan, M. Jin, Y. Luo, et al., "Field-Free Spin-Orbit Torque Switching in Synthetic Ferro and Antiferromagents with Exchange Field Gradient," *Advanced Functional Materials* 33 (2023): 2211953, https://doi.org/10.1002/adfm.202211953.

40. Y. W. Oh, S. H. Chris Baek, Y. M. Kim, et al., "Field-free Switching of Perpendicular Magnetization through Spin–orbit Torque in Antiferromagnet/Ferromagnet/Oxide Structures," *Nature Nanotechnology* 11 (2016): 878–884, https://doi.org/10.1038/nnano.2016.109.

41. J. Wei, X. Wang, B. Cui, et al., "Field-Free Spin–Orbit Torque Switching in Perpendicularly Magnetized Synthetic Antiferromagnets," *Advanced Functional Materials* 32 (2021): 2109455, https://doi.org/10.1002/adfm.202109455.

42. Y. C. Lau, D. Betto, K. Rode, J. M. Coey, and P. Stamenov, "Spin–orbit Torque Switching without an External Field Using Interlayer Exchange Coupling," *Nature Nanotechnology* 11 (2016): 758–762, https://doi.org/10.1038/nnano.2016.84.

43. W. He, C. Wan, C. Zheng, et al., "Field-Free Spin–Orbit Torque Switching Enabled by the Interlayer Dzyaloshinskii–Moriya Interaction," *Nano Letters* 22 (2022): 6857–6865, https://doi.org/10.1021/acs.nanolett.1c04786.

44. Z. Wang, P. Li, M. Fattouhi, et al., "Field-free Spin-orbit Torque Switching of Synthetic Antiferromagnet through Interlayer Dzyaloshinskii-Moriya Interactions," *Cell Reports Physical Science* 4 (2023): 101334, https://doi.org/10.1016/j.xcrp.2023.101334.

45. X. Zhao, L. Ji, W. Liu, et al., "Field-Free Switching of a Spin-Orbit-Torque Device through Interlayer-Coupling-Induced Domain Walls," *Physical Review Applied* 13 (2020): 044074, https://doi.org/10.1103/PhysRevApplied.13.044074.

46. J. Ryu, C. O. Avci, M. Song, et al., “Deterministic Current-Induced Perpendicular Switching in Epitaxial Co/Pt Layers without an External Field,” *Advanced Functional Materials* 33 (2023): 2209693, https://doi.org/10.1002/adfm.202209693.

47. A. Manchon, J. Železný, I. M. Miron, et al., “Current-induced Spin-orbit Torques in Ferromagnetic and Antiferromagnetic Systems,” *Reviews of Modern Physics* 91 (2019): 035004, https://doi.org/10.1103/RevModPhys.91.035004.

48. D. Kumar, T. Jin, R. Sbiaa, et al., “Domain Wall Memory: Physics, Materials, and Devices,” *Physics Reports* 958 (2022): 1–35, https://doi.org/10.1016/j.physrep.2022.02.001.

49. S. Yang, T. S. Ju, J. Seo, et al., “Ultralow-current Magnetization Switching in Nearly Compensated Synthetic Antiferromagnetic Frames Using Sandwiched Spin Sources,” *Acta Materialia* 208 (2021): 116708, https://doi.org/10.1016/j.actamat.2021.116708.

50. C. Fowley, N. Decorde, K. Oguz, K. Rode, H. Kurt, and J. M. D. Coey, “Perpendicular Magnetic Anisotropy in CoFeB/Pd Bilayers,” *IEEE Transactions on Magnetics* 46 (2010): 2116–2118, https://doi.org/10.1109/TMAG.2010.2044374.

51. P. Bruno and C. Chappert, “Oscillatory Coupling between Ferromagnetic Layers Separated by a Nonmagnetic Metal Spacer,” *Physical Review Letters* 67 (1991): 1602–1605, https://doi.org/10.1103/PhysRevLett.67.1602.

52. S. S. Parkin and D. Mauri, “Spin Engineering: Direct Determination of the Ruderman-Kittel-Kasuya-Yosida Far-field Range Function in Ruthenium,” *Physical Review B* 44 (1991): 7131–7134, https://doi.org/10.1103/PhysRevB.44.7131.

53. X. Zhao and J. Zhao, “Interlayer Dzyaloshinskii-moriya Interaction In Spintronics,” *npj Spintronics* 3 (2025): 25, https://doi.org/10.1038/s44306-025-00091-2.

54. D. S. Han, K. Lee, J. P. Hanke, et al., “Long-range Chiral Exchange Interaction in Synthetic Antiferromagnets,” *Nature Materials* 18 (2019): 703–708, https://doi.org/10.1038/s41563-019-0370-z.

55. A. Fernández-Pacheco, E. Vedmedenko, F. Ummelen, R. Mansell, D. Petit, and R. P. Cowburn, “Symmetry-breaking Interlayer Dzyaloshinskii–Moriya Interactions in Synthetic Antiferromagnets,” *Nature Materials* 18 (2019): 679–684, https://doi.org/10.1038/s41563-019-0386-4.

56. K. Wang, L. Qian, S. C. Ying, and G. Xiao, “Spin-orbit Torque Switching of Chiral Magnetization across a Synthetic Antiferromagnet,” *Communications Physics* 4 (2021): 10, https://doi.org/10.1038/s42005-020-00513-z.

57. W. He, C. Wan, C. Zheng, et al., “Field-Free Spin–Orbit Torque Switching Enabled by the Interlayer Dzyaloshinskii–Moriya Interaction,” *Nano Letters* 22 (2022): 6857–6865, https://doi.org/10.1021/acs.nanolett.1c04786.

58. X. He, Y. Sheng, J. Yun, et al., “Ion-irradiation-induced Field-free Magnetization Switching in Synthetic Antiferromagnets by Spin–orbit Torque,” *Journal of Magnetism and Magnetic Materials* 582 (2023): 170977, https://doi.org/10.1016/j.jmmm.2023.170977.

59. Y. Liu, B. Zhou, and J. G. Zhu, “Field-free Magnetization Switching by Utilizing the Spin Hall Effect and Interlayer Exchange Coupling of Iridium,” *Scientific Reports* 9 (2019): 325, https://doi.org/10.1038/s41598-018-37586-4.

60. H. Wu, S. A. Razavi, Q. Shao, et al., “Spin-orbit Torque from a Ferromagnetic Metal,” *Physical Review B* 99 (2019): 184403, https://doi.org/10.1103/PhysRevB.99.184403.

61. W. B. Liao, T. Y. Chen, Y. C. Hsiao, and C. F. Pai, “Pulse-Width and Temperature Dependence of Memristive Spin-Orbit Torque Switching,” *Applied Physics Letters* 117 (2020): 182402, https://doi.org/10.1063/5.0022257.

62. W. Chen, L. Qian, and G. Xiao, “Deterministic Current Induced Magnetic Switching without External Field Using Giant Spin Hall Effect of β-W,” *Scientific Reports* 8 (2018): 8144, https://doi.org/10.1038/s41598-018-26586-z.

63. S. Łazarski, W. Skowroński, K. Grochot, et al., “Spin-orbit Torque Induced Magnetization Dynamics And Switching in a Cofeb/ta/cofeb System With Mixed Magnetic Anisotropy,” *Physical Review B* 103 (2021): 134421, https://doi.org/10.1103/PhysRevB.103.134421.

64. C. Wu, Y. Wen, G. Zeng, et al., “Field-Free Spin-Orbit Torque Induced Magnetization Switching in Synthetic Antiferromagnet with Perpendicular Magnetic Anisotropy,” “Available at SSRN 4408694,” .

65. P. Dou, J. Zhang, Y. Guo, et al., “Deterministic Magnetization Switching via Tunable Noncollinear Spin Configurations in Canted Magnets,” *Nano Letters* 23 (2023): 6449–6457, https://doi.org/10.1021/acs.nanolett.3c01192.

66. X. Xie, X. Zhao, Y. Dong, et al., “Controllable Field-free Switching of Perpendicular Magnetization through Bulk Spin-orbit Torque in Symmetry-broken Ferromagnetic Films,” *Nature Communications* 12 (2021): 2473, https://doi.org/10.1038/s41467-021-22819-4.

67. D. Davis, “Thomas-Fermi Screening in One Dimension,” *Physical Review B* 7 (1973): 129–135, https://doi.org/10.1103/PhysRevB.7.129.

68. E. Piatti, D. Romanin, R. S. Gonnelli, and D. Daghero, “Anomalous Screening of an Electrostatic Field at the Surface of Niobium Nitride,” *Applied Surface Science* 461 (2018): 17–22, https://doi.org/10.1016/j.apsusc.2018.05.181.

69. Z. Chen, Q. Yang, L. Tao, and E. Y. Tsymbal, “Reversal of the Magnetoelectric Effect at a Ferromagnetic Metal/Ferroelectric Interface Induced by Metal Oxidation,” *npj Computational Materials* 7 (2021): 204, https://doi.org/10.1038/s41524-021-00679-2.

70. M. Zelený and I. Dlouhý, “Magnetism of Coherent Co and Ni Thin Films on Cu(111) and Au(111) Substrates: An ab Initio Study,” *Journal of Magnetism and Magnetic Materials* 424 (2017): 394, https://doi.org/10.1016/j.jmmm.2016.07.027.

71. E. Simon, L. Rózsa, K. Palotás, and L. Szunyogh, “Magnetism of a Co Monolayer on Pt(111) Capped by Overlayers of 5d Elements: A Spin-model Study,” *Physical Review B* 97 (2018): 134405, https://doi.org/10.1103/PhysRevB.97.134405.

72. K. S. Ryu, L. Thomas, S. H. Yang, and S. Parkin, “Chiral Spin Torque at Magnetic Domain Walls,” *Nature Nanotechnology* 8 (2013): 527–533, https://doi.org/10.1038/nnano.2013.102.

73. D. Stosic, T. B. Ludermir, and M. V. Milošević, “Pinning of Magnetic Skyrmions in a Monolayer Co Film on Pt(111): Theoretical Characterization and Exemplified Utilization,” *Physical Review B* 96 (2017): 214403, https://doi.org/10.1103/PhysRevB.96.214403.

74. G. Jan, L. Thomas, and S. Le, "Demonstration of Ultra-Low Voltage and Ultra low Power STT-MRAM Designed for Compatibility with 0x Node Embedded LLC Applications," in *2018 IEEE Symposium on VLSI Technology* (IEEE, 2018), 65–66, https://doi.org/10.1109/VLSIT.2018.8510672.

75. L. Thomas, G. Jan, and S. Serrano-Guisan, "Stt-Mram Devices With Low Damping and Moment Optimized for Llc Applications at Ox Nodes," in *IEEE International Electron Devices Meeting (IEDM)* (IEEE, 2018),27.3.1–27.3.4, https://doi.org/10.1109/IEDM.2018.8614700.

76. J. M. Iwata-Harms, G. Jan, S. Serrano-Guisan, et al., “Ultrathin Perpendicular Magnetic Anisotropy CoFeB Free Layers for Highly Efficient, High Speed Writing in Spin-transfer-torque Magnetic Random Access Memory,” *Scientific Reports* 9 (2019): 19407, https://doi.org/10.1038/s41598-019-54466-7.

77. A. S. Silva, S. P. Sá, S. A. Bunyaev, et al., “Dynamical Behaviour of Ultrathin [CoFeB (tCoFeB)/Pd] Films with Perpendicular Magnetic Anisotropy,” *Scientific Reports* 11 (2021): 43, https://doi.org/10.1038/s41598-020-79632-0.

78. L. Zhu, D. C. Ralph, and R. A. Buhrman, “Effective Spin-Mixing Conductance of Heavy-Metal–Ferromagnet Interfaces,” *Physical Review Letters* 123 (2019): 057203, https://doi.org/10.1103/PhysRevLett.123.057203.

79. R. Morgunov, A. Hamadeh, T. Fache, et al., "Magnetic Field and Temperature Control over Pt/Co/Ir/Co/Pt Multistate Magnetic Logic Device," *Superlattices and Microstructures* 104 (2017): 509–517, https://doi.org/10.1016/j.spmi.2017.02.033.

80. O. Koplak, A. Talantsev, Y. Lu, et al., "Magnetization Switching Diagram of a Perpendicular Synthetic Ferrimagnet CoFeB/Ta/CoFeB Bilayer," *Journal of Magnetism and Magnetic Materials* 433 (2017): 91–97, https://doi.org/10.1016/j.jmmm.2017.02.047.

81. S. Chen, Y. Xiao, W. H. Xie, Z. Zhang, B. Ma, and Q. Y. Jin, "Interfacial Effects on Magnetic Interlayer Coupling between Perpendicular Co/Ni Multilayers across Ru Spacer," *Applied Physics Letters* 105 (2014): 262403, https://doi.org/10.1063/1.4905244.

82. A. Thiaville, S. Rohart, É. Jué, V. Cros, and A. Fert, "Dynamics of Dzyaloshinskii Domain Walls in Ultrathin Magnetic Films," *EPL (Europhysics Letters)* 100 (2012): 57002, https://doi.org/10.1209/0295-5075/100/57002.

83. S. Emori, U. Bauer, S. M. Ahn, E. Martinez, and G. S. Beach, "Current-driven Dynamics of Chiral Ferromagnetic Domain Walls," *Nature Materials* 12 (2013): 611–616, https://doi.org/10.1038/nmat3675.

84. M. J. Meijer, J. Lucassen, O. Kurnosikov, et al., "Magnetic Chirality Controlled by the Interlayer Exchange Interaction," *Physical Review Letters* 124 (2020): 207203, https://doi.org/10.1103/PhysRevLett.124.207203.

85. X. Wang, H. Wu, R. Qiu, et al., "Room Temperature Field-free Switching of CoFeB/MgO Heterostructure Based on Large-scale Few-layer WTe_2," *Cell Reports Physical Science* 4 (2023): 101468, https://doi.org/10.1016/j.xcrp.2023.101468.

86. X. Zhang, W. Cai, M. Wang, et al., "Spin-Torque Memristors Based on Perpendicular Magnetic Tunnel Junctions for Neuromorphic Computing," *Advanced Science* 8 (2021): 2004645, https://doi.org/10.1002/advs.202004645.

87. N. Murray, W. B. Liao, T. C. Wang, et al., "Field-free Spin-orbit Torque Switching through Domain Wall Motion," *Physical Review B* 100 (2019): 104441, https://doi.org/10.1103/PhysRevB.100.104441.

88. Z. Zhao, A. K. Smith, M. Jamali, and J. P. Wang, "External-Field-Free Spin Hall Switching of Perpendicular Magnetic Nanopillar with a Dipole-Coupled Composite Structure," *Advanced Electronic Materials* 6 (2020): 1901368, https://doi.org/10.1002/aelm.201901368.

Supporting Information

Additional supporting information can be found online in the Supporting Information section.

Supporting File: adfm77784-sup-0001-SuppMat.docx.